ELSEVIER

Contents lists available at ScienceDirect

Journal of Fluids and Structures

journal homepage: www.elsevier.com/locate/jfs



Aeroelastic interactions and trajectory selection of vortex gusts impinging upon Joukowski airfoils



Huansheng Chen*, Justin W. Jaworski

Department of Mechanical Engineering and Mechanics, Lehigh University, Bethlehem, PA, 18015, United States of America

ARTICLE INFO

Article history:
Received 28 July 2019
Received in revised form 10 February 2020
Accepted 1 May 2020
Available online xxxx

Keywords: Conformal mapping Aeroelastic gust response Point vortex dynamics Brown and Michael equation

ABSTRACT

The dynamically-coupled interactions of vortex gusts encountering a symmetric Joukowski airfoil on linear elastic supports is formulated analytically and evaluated numerically using a time-dependent conformal mapping. The Brown and Michael framework models the unsteady shedding of vorticity from the airfoil into the wake, and the aeroelastic motion of the airfoil is analyzed using quasi-steady, apparent mass, and fully-unsteady aerodynamic models. Special attention is paid to the influences of the strength of the incident vortex and the airfoil natural frequency on the initial upstream placement of a vortex gust that achieves direct impingement. These results are weakly sensitive to the initial vortex position in the limits of either large or small structural natural frequency, and the initial vertical vortex position to achieve impingement changes monotonically with the vortex strength. A comparison of the numerical model with available experimental vortex gust measurements over stationary airfoils highlights the appropriate use of the point-vortex model for inviscid vortex-airfoil interaction problems without significant vortex strength decay, which occurs for predominantly viscous interactions of close vortex-airfoil encounters.

© 2020 Elsevier Ltd. All rights reserved.

1. Introduction

The encounter of a vortex gust with an aerodynamic body is a canonical fluid–structure interaction with implications for the prediction of transient loads on fliers and swimmers and their generation of vortex sound. Among the various orientations that the incident vortex can take with respect to the solid body (cf. Rockwell (1998)), the alignment of the spanwise vortex with the orientation of the bound vorticity on the body, the wake, and the boundary-layer vorticity allows for their dynamic coupling during a vortex–airfoil encounter. For this reason, a number of theoretical, numerical, and experimental studies have been carried out to understand and model two-dimensional vortex–structure interactions.

Many prior investigations of two-dimensional vortex-body interactions consider static solid structures, where the flow unsteadiness arises from the motion of one or many coherent vortices. The simplest analytical models of these scenarios represent the vortex structures as point vortices, where the solid boundaries are often transformed via conformal mapping techniques to simple geometries where the solution is known or is easily determined. Analytical vortex-structure modeling has historically focused on the effects of boundary geometry on the vortex path, which is of interest to gain insight into the evolution of coherent flows and is critical in the assessment of vortex sound generation (Crighton, 1972; Howe, 1997; Conlisk and Veley, 1985; Jaworski, 2016, 2018, 2019). These analytical models can be generalized to handle

E-mail addresses: huc216@lehigh.edu (H. Chen), jaworski@lehigh.edu (J.W. Jaworski).

^{*} Corresponding author.

multiply-connected domains (Baddoo and Ayton, 2018; Crowdy, 2010), as well as vortex clouds (Panaras, 1987) or finite-sized vortices (Newton, 2013). The close encounter of real vortices with surface nonuniformities (e.g., an edge, corner, or surface asperity) and the large surface pressure fluctuations they can impart are sensitive to the incoming vortex strength (Conlisk and Rockwell, 1981), the geometrical details of the boundary (Rockwell and Knisely, 1979), and the alignment of the vortex with the solid body (Conlisk and Rockwell, 1981; Ziada and Rockwell, 1982; Gursul and Rockwell, 1990). To date, analytical investigations of direct vortex impingement have not been developed for structures under aeroelastic motions, which is a key contribution of the present study.

The local vortex-body interaction of near or direct impingement can lead to significant distortion of the incoming vortex (Gursul and Rockwell, 1990) and its possible severing by the body into two parts (Rockwell and Knisely, 1979; Lee and Smith, 1991; Barnes and Visbal, 2018a,b). Strong viscous and nonlinear effects in the neighborhood of the solid boundary can also lead to transient separation and turbulent transition of the surface boundary layer (Barnes and Visbal, 2018a,b), the eruption of vorticity from this boundary layer (Doligalski et al., 1994), the creation of additional vortices (Ziada and Rockwell, 1982), and a time-dependent change in the circulation of the incident vortex gust (Peng and Gregory, 2015). It is argued in the present work (along the lines of Rogler (1978)) that regimes with significant viscous interaction between the incident vortex and boundary layer indicate the practical limit of point-vortex models for aeroelastic vortex gust simulations.

Dynamic structural motions affect the paths of the incident vortex and the vorticity shed into the wake, which is the product of unsteady loading by the vortex gust on the aerodynamic structure or airfoil. These structural motions may be either prescribed (Manela, 2013) or the result of aeroelastic coupling with the vortex gust, where in the latter case the compliance of either the airfoil or its support provides the means for a dynamic two-way energy transfer between the fluid and the solid body. The introduction of structural elasticity into the physical system leads to the possibility of resonance effects, which have been studied in the context of flow noise amplification and suppression by Howe (1994) for a turbulent inflow and by Manela (2011) for a point-vortex gust. Aeroelastic point-vortex interactions have lacked attention in the literature in comparison to cases with static structures or prescribed motion. Manela and Huang (2013) investigated the interaction of an incident point vortex with a trailing edge flap mounted to a torsional spring, and Riso et al. (2016) investigated impulsive and transient gust loads using a discrete free wake with vortices shed at every instant in time. These studies were carried out for flat plates and did not consider the effects of airfoil geometry on the vortex-structure interaction. The present work is motivated by the need to assess this geometrical effect in addition to the dynamically-coupled interactions of the incident vortex, the aeroelastic airfoil motion, and the vortex wake.

The production and evolution of vorticity shed into the wake determines the unsteady aerodynamic load on an airfoil. Accordingly, researchers have sought to develop low-order models for unsteady vortex shedding that are accurate with respect to load prediction and can also provide physical insight into the flow field at a modest computational cost relative to a full numerical simulation of the Navier-Stokes equations. Early wake models for transient airfoil motions (von Kármán and Sears, 1938; Bisplinghoff et al., 1996) supposed a flat, continuous vortex sheet that is appropriate for small-amplitude airfoil motions but becomes increasingly inaccurate for large-amplitude airfoil motions or severe gust responses (Riso et al., 2016). Brown and Michael (1954, 1955) and Edwards (1954) developed independently a point-vortex model to describe the static vortices positioned over lifting delta wings due to leading-edge separation. This model was adapted by Cheng (1954) and Rott (1956) for unsteady two-dimensional flow with point vortices whose strengths are allowed to vary in time. The Brown and Michael model framework supposes that the vorticity shed from an edge rolls up via a connecting vortex sheet into a concentrated point vortex, whose strength is set by the Kutta condition and whose position is described by a first-order differential equation: the so-called Brown and Michael equation. The original model formulation brought about a spurious surface force on the airfoil that was identified by Peters and Hirschberg (1993) and was eliminated by Howe (1996) in his emended form of the Brown and Michael equation, which is used in the present work. Michelin and Llewellyn Smith (2009) reviewed and formalized the derivation of the Brown and Michael equation, which results from a linear momentum balance requiring zero net force on both the shed vortex and on the connecting vortex sheet. However, Michelin and Llewellyn Smith (2009) pointed out that the Brown and Michael framework has an insufficient number of free parameters to impose both linear and angular momentum balances on the vortex and the connecting sheet, in addition to the condition that the strength of a trailing-edge point vortex cannot decrease in time. Wang and Eldredge (2013) built upon the conservation of impulse argument by Tchieu and Leonard (2011) to develop a new evolution model for shed point vortices that agrees well with airfoil simulations at high pitch rates with shedding from both leading and trailing edges. More recently, Darakananda and Eldredge (2019) developed a hybrid modeling approach where the rate at which the vortex sheets roll up into point vortices may be adjusted by the analyst to gain the desired level of physical insight into the fluid dynamics. Eldredge and Jones (2019) provided a full contemporary review of low-order approaches to vortex modeling.

The objective of the present work is to model the dynamic vortex-gust interactions of non-flat airfoils that are mounted to a linear suspension. The theoretical model is used to investigate the dynamic interplay between a vortex gust, unsteady vortex shedding, the airfoil shape, and the aeroelastic airfoil motion, as well as to predict the conditions for direct vortex impingement. To these ends, Section 2 develops the mathematical model and dynamic formulation for vortex-gust interactions with a Joukowski airfoil. Section 3 first studies the effect of airfoil thickness and compares the model results against previous experiments with fixed airfoils. The dimensionless aeroelastic parameters and the initial placement of the vortex gust to achieve direct airfoil impingement are then determined numerically. Section 4 summarizes the results from this study and presents concluding remarks.

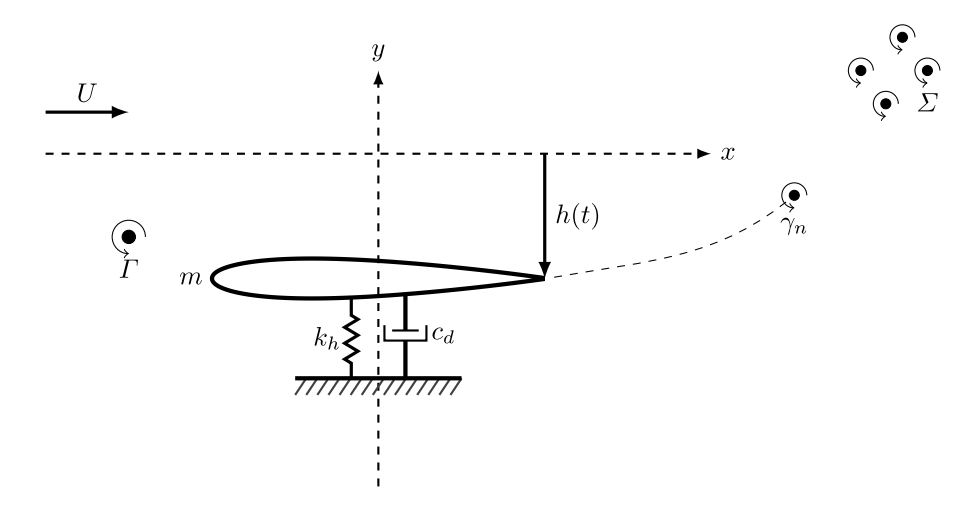


Fig. 1. Schematic of the generalized model problem of an incident vortex interaction with a symmetric Joukowski airfoil on elastic translational support in a uniform flow, where U is the flow speed and h(t) denotes the downward plunge displacement of the airfoil. The coordinate system passes through the airfoil midchord at x=0. The airfoil can be considered as a damped harmonic oscillator with mass m, damping coefficient c_d , and spring stiffness k_h . Γ denotes the strength of the incident line vortex, and γ_n is the strength of the tethered trailing-edge vortex whose motion is determined by the emended Brown and Michael equation. Σ is the set of free vortices generated at the airfoil trailing edge due to unsteady airfoil loads in response to the incident line vortex or the airfoil motion. The airfoil has zero angle of attack. Vortex circulation is positive in the counterclockwise orientation.

2. Mathematical formulation

Fig. 1 illustrates the model problem of a Joukowski airfoil on elastic supports in two-dimensional uniform flow with an incident line vortex Γ and the vorticity field Σ shed into the wake. All vortices are defined to have positive circulation in the counterclockwise direction. The strength of the trailing-edge vortex γ_n satisfies the Kutta condition, and its motion obeys the emended Brown and Michael equation (Howe, 1996). The mathematical formulation of the aeroelastic system is now described.

2.1. Mapping

The conformal mapping of the Joukowski airfoil between the physical z-plane and the mapped ζ -plane is described by

$$\zeta(z) = \frac{1}{2} \left(z + \sqrt{z^2 - 4\lambda^2} \right) - f_0,$$
 (1)

where f_0 is the origin of the unit circle in the f-plane, as shown in Fig. 2, and λ is the transformation parameter of the conformal mapping defined by $\lambda = \sqrt{r^2 - f_{y0}^2} - f_{x0}$. Using Eq. (1), the Joukowski airfoil in the physical z-plane (z = x + iy) with its trailing edge located at (2λ , 0) is mapped to a circle with radius r = 1 in the f-plane ($f = f_1 + if_2$), as shown in Fig. 2. Note the offset of the circle center at $f_0 = f_{x0} + if_{y0}$ and the corresponding trailing edge at (λ , 0). For the symmetric Joukowski airfoils considered in this work, $f_{y0} = 0$. The unit circle in the f-plane is then shifted by an elementary mapping to the origin in the ζ -plane.

When time-dependent airfoil motions are considered, Eq. (1) becomes

$$\zeta(s) = \frac{1}{2} \left[s(z, t) + \sqrt{s^2 - 4\lambda^2} \right] - f_0, \tag{2}$$

where s(z,t) = z - ih(t). The airfoil displacement h(t) may be either prescribed or be part of the solution in the case of aeroelastic airfoil motions.

2.2. Flow complex potential

The complex potential of the flow is

$$w(\zeta) = w_{\gamma} + w_{\Gamma} + w_{h} + U\left(\zeta + f_{0} + \frac{\lambda^{2}}{\zeta + f_{0}}\right), \tag{3}$$

where $w_{\gamma}(\zeta)$, $w_{\Gamma}(\zeta)$, and $w_{\hbar}(\zeta)$ are the complex potential contributions due to the shed and free vorticity field, the incident vortex, and the airfoil motion, respectively. The last term of Eq. (3) represents the uniform background flow.

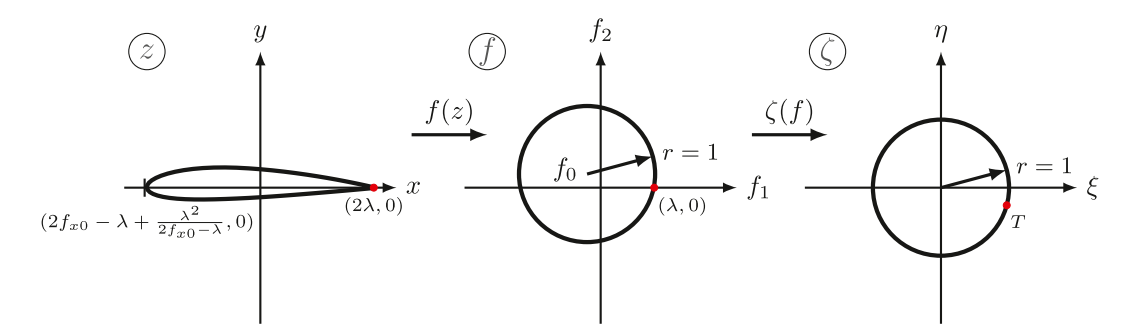


Fig. 2. Successive mappings of a generalized Joukowski airfoil in the physical *z*-plane to a unit circle centered at the origin in the *ζ*-plane. The red dot indicates the position of the trailing edge through successive mappings and is located at the complex-valued position *T* in the *ζ*-plane.

The complex potential $w_{\Gamma}(\zeta)$ of the incident vortex located instantaneously at ζ_{Γ} is determined from the model of a vortex moving around a cylinder (Howe, 2003), which yields

$$w_{\Gamma}(\zeta) = -\frac{i\Gamma}{2\pi} \log\left(\zeta - \zeta_{\Gamma}\right) + \frac{i\Gamma}{2\pi} \log\left(\zeta - \frac{1}{\zeta_{\Gamma}^{*}}\right) - \frac{i\Gamma}{2\pi} \log\zeta,\tag{4}$$

where the last two terms guarantee that the total circulation inside the cylinder is initially zero, and the asterisk denotes the complex conjugate. Similarly, the complex potential of the n vortices shed into the wake and located at positions ζ_{γ_n} is

$$w_{\gamma}(\zeta) = \sum_{k=1}^{n} \left[-\frac{i\gamma_{k}}{2\pi} \log\left(\zeta - \zeta_{\gamma_{k}}\right) + \frac{i\gamma_{k}}{2\pi} \log\left(\zeta - \frac{1}{\zeta_{\gamma_{k}}^{*}}\right) \right]. \tag{5}$$

By appeal to Kelvin's theorem, the bound vorticity inside the cylinder at any time has total circulation $-\sum_{k=1}^{n} \gamma_k$, which is used to compute the aerodynamic lift force.

The complex potential of the airfoil motion is Batchelor (1967)

$$w_h(\zeta) = iV\left(\zeta - \frac{1}{\zeta}\right),\tag{6}$$

where V = dh/dt is the instantaneous velocity of the airfoil in the downward direction.

2.3. Vortex shedding and the emended Brown and Michael equation

The motions of the shed vortices are described by the emended Brown and Michael equation (Howe, 1996),

$$\frac{\mathrm{d}\mathbf{x}_{\gamma_n}}{\mathrm{d}t} \cdot \nabla \Psi_j + \frac{\Psi_j}{\gamma_n} \frac{\mathrm{d}\gamma_n}{\mathrm{d}t} = \mathbf{v}_{\gamma_n} \cdot \nabla \Psi_j, \qquad j = 1, 2, \tag{7}$$

where \mathbf{x}_{γ_n} denotes the position of the *n*th shed vortex with circulation γ_n that is tethered to the trailing edge, and \mathbf{v}_{γ_n} is the fluid velocity when the self-induced local velocity of γ_n is excluded. A Cartesian coordinate system is used, where $\mathbf{x} \equiv (x, y)$. $\Psi_j(\mathbf{x}, t)$ denotes the stream function of the complex potential of the flow in the *j*-direction. For a Joukowski airfoil mapped to the ζ -plane, the components of the stream function are Howe (2014)

$$\Psi_1 = \operatorname{Im}\left\{\zeta + \frac{1}{\zeta}\right\} \quad \text{and} \quad \Psi_2 = \operatorname{Im}\left\{-i\left(\zeta - \frac{1}{\zeta}\right)\right\}.$$
(8)

The instantaneous circulation of the tethered vortex $\gamma_n(t)$ is obtained by enforcing the Kutta condition at the trailing edge of each instant in time,

$$\gamma_{n}(t) = \frac{\left|T^{*}\zeta_{\gamma_{n}} - 1\right|^{2}}{\left|\zeta_{\gamma_{n}}\right|^{2} - 1} \left(\frac{2\Gamma\left(1 - \operatorname{Re}\left\{T^{*}\zeta_{\Gamma}\right\}\right)}{\left|T^{*}\zeta_{\Gamma} - 1\right|^{2}} - \sum_{k=1}^{n-1} \gamma_{k} \frac{\left|\zeta_{\gamma_{k}}\right|^{2} - 1}{\left|T^{*}\zeta_{\gamma_{k}} - 1\right|^{2}} - 2\pi V \operatorname{Re}\left\{T^{*}\right\}\right),\tag{9}$$

in which T^* is the complex conjugate of the trailing edge T location ($T = \lambda - f_0$) in the ζ -plane. The tethered trailing-edge vortex is released and becomes a free vortex when $\mathrm{d}\gamma_n/\mathrm{d}t$ changes sign, at which time another tethered vortex is placed at the airfoil trailing edge whose motion and instantaneous circulation are determined by Eqs. (7) and (9), respectively (Howe, 1996; Graham, 1977, 1980). As described by Michelin and Llewellyn Smith (2009), this criterion for vortex shedding is based on the physical argument that the intensity of the point vortex cannot decrease in value, else it would imply a negative diffusion in the point vortex.

Eq. (7) can be rearranged into the equivalent scalar form

$$\frac{dz_{\gamma_n}^*}{dt} + (H_1 - iH_2) \frac{1}{\nu_n} \frac{d\gamma_n}{dt} = v_{\gamma_n}^*,$$
(10)

where $z_{\gamma_n}^* = x - iy$ and $v_{\gamma_n}^* = v_x - iv_y$. The functions H_1 and H_2 involve the stream functions Ψ_j and their derivatives. Eq. (10) is the equivalent scalar form of the emended Brown and Michael equation, which is employed for the theoretical analysis in this work. Specific details related to the derivation of Eq. (10) and the expressions of H_1 and H_2 from Chen and Jaworski (2018) are presented in Appendix A. Also,

$$v_{\gamma_n}^* = -\frac{i\gamma_n \zeta''(z_{\gamma_n})}{4\pi \zeta'(z_{\gamma_n})} + F_{\gamma_n}'(z_{\gamma_n}), \tag{11}$$

is the complex velocity of the shed vortex with self-potential velocity excluded (Howe, 2003). The first term on the right side of Eq. (11) is the so-called Routh correction (Clements, 1973), and the second term is the desingularized complex velocity at z_{ν_n} ,

$$F'_{\gamma_n}(z_{\gamma_n}) = \zeta' \left[\frac{\mathrm{d}w}{\mathrm{d}\zeta} + \frac{i\gamma_n}{2\pi} \frac{1}{\zeta - \zeta_{\gamma_n}} \right]. \tag{12}$$

2.4. Kinematics of the incident and free vortices

Similarly, the complex velocity of the incident line vortex at s_{Γ} is Howe (2003)

$$\frac{\mathrm{d}s_{\Gamma}^*}{\mathrm{d}t} = -\frac{i\Gamma\zeta''(s_{\Gamma})}{4\pi\zeta'(s_{\Gamma})} + F'(s_{\Gamma}),\tag{13}$$

where

$$F_{\Gamma}'(s_{\Gamma}) = \frac{i\Gamma}{2\pi} \frac{\zeta_{\Gamma}'}{(\zeta_{\Gamma}^2 - 1)\zeta_{\Gamma}} - \frac{i\zeta_{\Gamma}'}{2\pi} \sum_{k=1}^{n} \gamma_k \left(\frac{1}{\zeta_{\Gamma} - \zeta_{\gamma_k}} - \frac{1}{\zeta_{\Gamma} - 1/\zeta_{\gamma_k}^*} \right) + iV\zeta_{\Gamma}' \left(1 + \frac{1}{\zeta_{\Gamma}^2} \right) + U.$$

$$(14)$$

Note that $\zeta_{\Gamma} = \zeta_{\Gamma}(s)$ and $\zeta_{\gamma_k} = \zeta_{\gamma_k}(s)$. Also, the equation of motion for each of the n-1 free vortices is

$$\frac{\mathrm{d}s_{\gamma_k}^*}{\mathrm{d}t} = -\frac{i\gamma_k\zeta''(s_{\gamma_k})}{4\pi\zeta'(s_{\gamma_k})} + F_{\gamma_k}'(s_{\gamma_k}),\tag{15}$$

where

$$F'_{\gamma_{k}}(s_{\gamma_{k}}) = \frac{i\Gamma}{2\pi} \zeta'_{\gamma_{k}} \left(\frac{1}{\zeta_{\gamma_{k}} - \zeta_{\Gamma}} - \frac{1}{\zeta_{\gamma_{k}} - 1/\zeta_{\Gamma}^{*}} + \frac{1}{\zeta_{\gamma_{k}}} \right) + \frac{i\gamma_{k}}{2\pi} \frac{\zeta'_{\gamma_{k}}}{\zeta_{\gamma_{k}} - 1/\zeta_{\gamma_{k}}^{*}} - \frac{i\zeta'_{\gamma_{k}}}{2\pi} \sum_{m=1, m \neq k}^{n} \gamma_{m} \left(\frac{1}{\zeta_{\gamma_{k}} - \zeta_{\gamma_{m}}} - \frac{1}{\zeta_{\gamma_{k}} - 1/\zeta_{\gamma_{m}}^{*}} \right) + iV\zeta'_{\gamma_{k}} \left(1 + \frac{1}{\zeta_{\gamma_{k}}^{2}} \right) + U.$$
(16)

2.5. Airfoil motion and loads

The airfoil moves aeroelastically under its lift force and the equation of motion of the elastic mount,

$$m\frac{d^{2}h}{dt^{2}} + c_{d}\frac{dh}{dt} + k_{h}h = -L', \tag{17}$$

where h(t) denotes the plunge displacement of the airfoil with chord length c. The elastic suspension can be considered as a damped harmonic oscillator with airfoil mass m, damping coefficient c_d , and spring stiffness k_h . The unsteady sectional lift force L' on a thin airfoil is determined by Katz and Plotkin (2001)

$$L' = \rho U \Gamma_a(t) + \rho \int_0^c \frac{\partial}{\partial t} \Gamma_a(x, t) \, \mathrm{d}x \,, \tag{18}$$

where the airfoil circulation $\Gamma_a(t)$ is the integrated vorticity bound to the airfoil, $\Gamma_a = \int_0^c \gamma(x,t) dx$. The first term is the quasi-steady Kutta-Joukowski lift due to the instantaneous circulation, and the second term includes the unsteady contributions to the lift due to the fluid loading on the airfoil (added mass) and the downwash effect of the wake.

The instantaneous circulation Γ_a is determined by Kelvin's theorem,

$$\Gamma_a(t) = -\sum_{k=1}^n \gamma_k(t),\tag{19}$$

where γ_k denotes the strength of the *k*th shed vortex. The airfoil vorticity distribution may be rewritten analytically as a trigonometric expansion of the following form (Glauert, 1983):

$$\gamma(\theta, t) = 2U \left[A_0(t) \frac{1 + \cos \theta}{\sin \theta} + \sum_{n=1}^{\infty} A_n(t) \sin n\theta \right], \tag{20}$$

where the first term in the bracket is the vorticity distribution for the symmetric airfoil, and the second term summation represents the camber distribution. Note that for symmetric airfoils with zero angle of attack, as considered in the present work, $A_1 = A_2 = A_3 = \ldots = A_n = 0$, and only $A_0(t)$ is not identically zero at all times. Eq. (18) can be expanded as

$$L' = \pi \rho c U^2 A_0 + \pi \rho c^2 U \frac{3}{4} \frac{\partial A_0}{\partial t},\tag{21}$$

where the first term is equivalent to the quasi-steady lift in Eq. (18), and the second term is equivalent to the lift contribution due to time dependency. Details of this expansion can be found in Katz and Plotkin (2001).

The system of dynamical equations is formed from Eqs. (9), (10), (13), (15), and (21), which consists of 2(n + 2) first-order ordinary differential equations for the position $(s_{X_T}(t), s_{Y_T}(t))$ of the incident line vortex, the positions $(s_{X_T}(t), s_{Y_T}(t))$ of n trailing-edge vortices, and the instantaneous airfoil displacement h(t) and the plunging velocity V(t). The system of equations is marched forward in time using ODE45 in MATLAB, where the relative and absolute solution tolerances are set to 10^{-8} . Once solved, the results are mapped to the physical z-plane using z(t) = s(t) + ih(t).

3. Results

The numerical framework developed in Section 2 is verified against Manela (2013) in the limiting cases of a flat plate that is either stationary or under prescribed harmonic plunging motions; further details of this verification are provided in Appendix B. New results are now presented to examine the effect of airfoil thickness on gust interactions with stationary bodies. These results are compared against the gust experiments conducted by Peng and Gregory (2015, 2017) to assess the predictive limitations of the present theory. Aeroelastic gust–airfoil interactions are then explored, and the upstream vortex conditions to achieve direct impingement are determined numerically.

The model problem is nondimensionalized by $\bar{x}=x/(2\lambda)$, $\bar{y}=y/(2\lambda)$, $\bar{t}=Ut/(2\lambda)$, and $\bar{\Gamma}=\Gamma/(4\pi U\lambda)$. All simulations are initialized with the initial trailing-edge vortex positioned at $\bar{z}_{\gamma}(0)=z_{\gamma}(0)/(2\lambda)=(1,10^{-6})$. Unless otherwise stated, the initial horizontal position of the vortex gust is $\bar{x}_{\Gamma}(0)=\text{Re}\{\bar{z}_{\Gamma}(0)\}=-20$. Note that the dimensionless parameters in Section 3.2 follow those used by Peng and Gregory (2015, 2017) for the sake of comparison and are slightly different from the parameters in other sections. The circle centers of the symmetric airfoils considered herein require $f_{y0}=0$.

3.1. Effect of airfoil thickness on vortex-gust interaction

The effect of airfoil thickness on a vortex gust interaction with a stationary, symmetric Joukowski airfoil is now examined. The time histories of the bound circulation and the trajectories of the incident and shed trailing-edge vortices are investigated as a function of airfoil thicknesses. Joukowski airfoils with thickness-to-chord ratios of 0%, 12%, 20%, and 25% corresponded to the mapped circle in the f-plane centered at horizontal positions $f_{\chi 0} = \{0, -0.092, -0.155, -0.2\}$, respectively. The initial vertical vortex location is $\overline{y}_{\Gamma}(0) = \text{Im}\{\overline{z}_{\Gamma}(0)\} = 0.2$, and the vortex strength is $\overline{\Gamma} = 0.2$. This nondimensional vortex strength is selected to match the numerical simulations by Manela (2013) for the special case of a fixed flat plate airfoil. Details of this verification are presented in Appendix B.

The numerical simulations produce three trailing-edge vortices as a result of gust encounter for all airfoil thickness considered, which also occurs in the case of a stationary flat plate (Manela, 2013). Fig. 3 compares the trajectories of the incident vortex Γ and shed vortices γ_1 , γ_2 , and γ_3 for increasing values of airfoil thickness. The trajectories of γ_1 , γ_2 , γ_3 , and Γ all have a similar shape for different values of the airfoil thickness, where greater deviations are observed at long times for larger airfoil thicknesses. The comparison of airfoil circulation for each case is shown in Fig. 4. Despite minor differences in the airfoil circulation for different cases, larger airfoil thicknesses lead to larger peak-to-peak values of airfoil circulation and may result in larger sectional lift coefficients in the course of a vortex gust encounter.

3.2. Model comparison against experiments

The analytical–numerical model in this work permits comparisons of the present scheme against vortex gust experiments for non-flat airfoils that are available in the literature. Here, a comparison is made with an experimental study by Peng and Gregory (2015) on the interaction of an incident vortex with a stationary NACA0012 airfoil in a uniform flow.

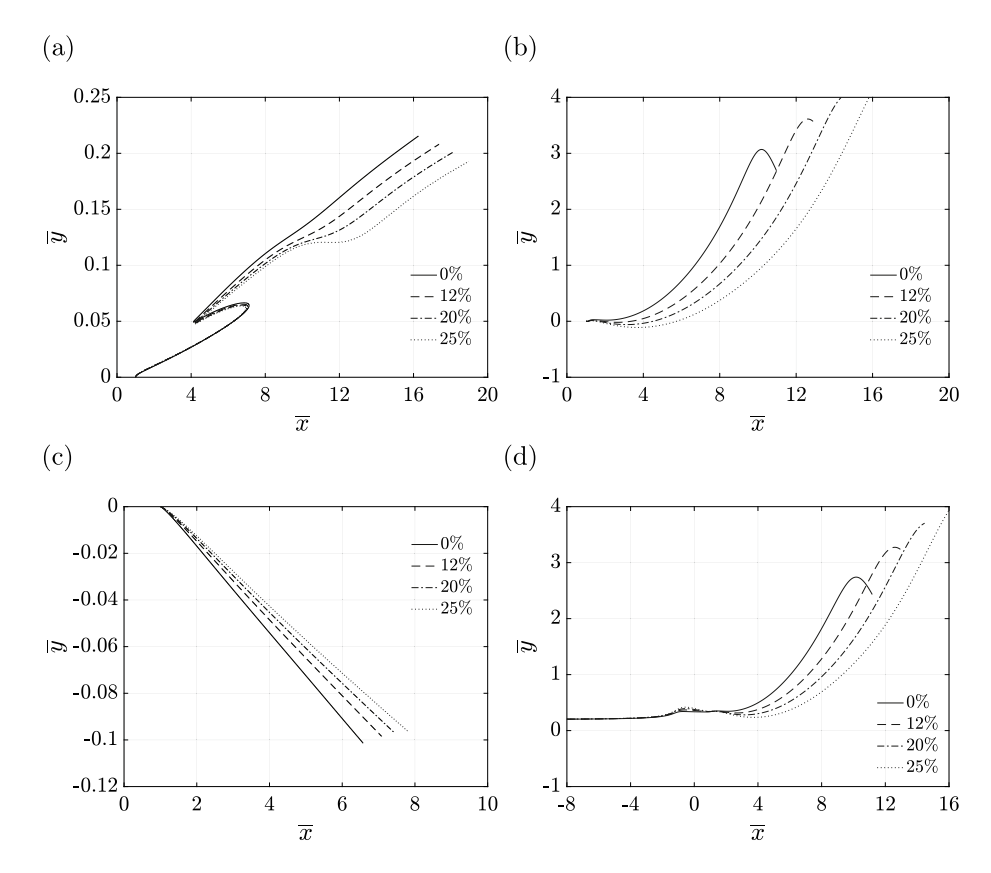


Fig. 3. Effects of thickness-to-chord ratio on the trajectories of an incident line vortex Γ and the three shed vortices γ_1 , γ_2 , and γ_3 resulting from its encounter with a stationary Joukowski airfoil in uniform flow with zero angle of attack: (a) trajectories of trailing edge vortex γ_1 ; (b) trajectories of trailing edge vortex γ_2 ; (c) trajectories of trailing edge vortex γ_3 ; (d) trajectories of incident vortex Γ . Initial vertical vortex position $\bar{y}_{\Gamma}(0) = 0.2$ and vortex strength $\bar{\Gamma} = 0.2$.

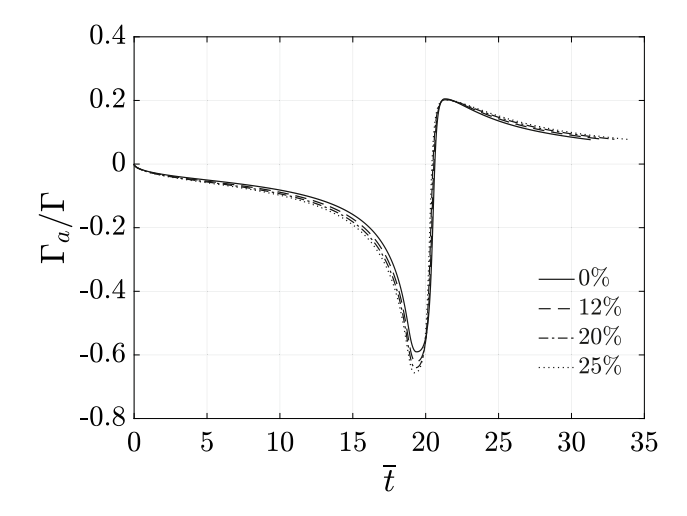


Fig. 4. Time histories of scaled bound circulation of a vortex gust encounter with a stationary airfoil as a function of thickness-to-chord ratio. Initial vertical vortex position $\bar{y}_{\Gamma}(0) = 0.2$ and vortex strength $\bar{\Gamma} = 0.2$.

Their study tracked the change in the incident vortex strength due to its encounter with the airfoil in addition to the trajectory of this vortex as a function of the initial vertical vortex positions.

To furnish a comparison, the present numerical simulations use a symmetric Joukowski airfoil with 12% thickness, where $f_{x0} = -0.092$. Since the present area of interest is the parabolic airfoil leading edge, small differences in airfoil

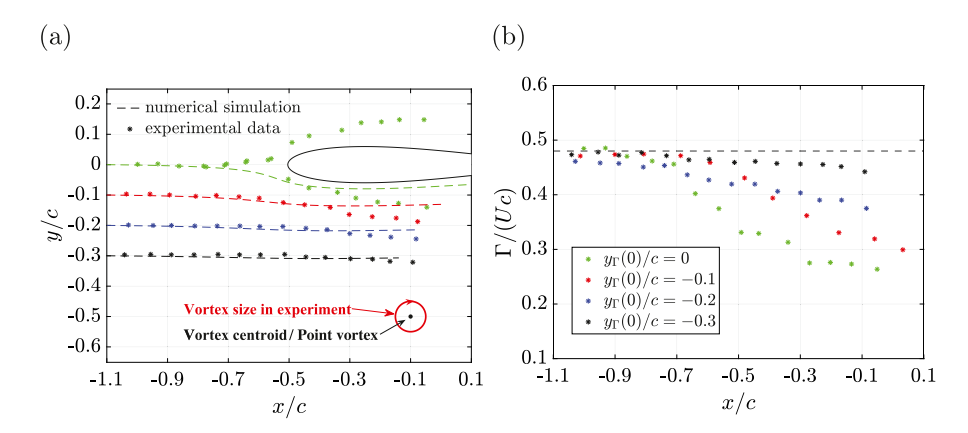


Fig. 5. Comparison of incident vortex gust trajectory near a 12% thickness airfoil against the experiments data of Peng and Gregory (2015, Fig. 16) for $\Gamma/(Uc) = -0.48$ (clockwise). The nondimensional vortex strength in the numerical simulation matches the value in the experiments prior to the airfoil encounter. (a) Dependence of vortex trajectory on initial vortex placement. Splitting occurs for experiments with the vortex aligned with the airfoil. The radius of the vortex core in the experiment is 0.1c. (b) Variation of the vortex strength as a function of initial position and downstream locations. The point vortex does not change its initial strength and is denoted by the dashed line. Asterisks denote averaged experimental data. (For interpretation of the references to color in this figure legend, the reader is referred to the web version of this article.)

shape are negligible in this comparison. The dimensionless initial vertical locations are $y_{\Gamma}(0)/c = \{0, -0, 1, -0.2, -0.33\}$, where the chord length of the airfoil is related to λ by the expression $c = 3\lambda - 2f_{x0} - \lambda^2/(2f_{x0} - \lambda)$. For a NACA0012 airfoil, $c/\lambda \approx 4.034$. The strength of the incoming vortex is matched with the experiments with $\Gamma/(Uc) = -0.48$ (clockwise). It is worth noting that the vortex strength does not change in the current analytic work due to its representation as a point vortex.

Fig. 5 compares results from the current inviscid model simulations with available experimental measurements. The experimental results are denoted by asterisks whose different colors correspond to various vortex positions, and the associated simulation results are indicated by dashed lines. For initial vortex locations $v_{\mathcal{L}}(0)/c = -0.2$ (blue), and -0.3 (black), the numerical and experimental results for trajectories agree when the vortex is far from the airfoil. Small deviations of the vortex trajectory results are observed once the vortex passes beyond x/c > -0.3, which is likely due to the displacement effect of the airfoil boundary layer. However, for initial vortex position $v_{\Gamma}(0)/c = \{-0.1, 0\}$, large deviations are observed between the predicted vortex trajectories of the numerical simulation and the experimental data when the vortex is close to the airfoil. As shown in Fig. 5(b), Peng and Gregory (2015) report a significant (30% to 40%) drop in vortex strength due to deceleration effects of the strong adverse pressure gradient near the leading-edge of the airfoil, where the vortex decay may not be sufficient to explain completely the large deviations of the vortex trajectories. A collision of the vortex with the airfoil leading-edge is observed in the experiment when the initial incident vortex location is $y_{\Gamma}(0)/c = 0$. In this case, the incident vortex with a finite core radius of 0.1c is split by the airfoil leading edge, as shown in Fig. 5(a), Clearly, the point vortex model in the inviscid numerical simulation cannot represent the physics associated with finite vortex cores nor any viscous-inviscid interactions between the vortex and airfoil. Thus, our inviscid simulation model cannot predict the experimental trends in vortex strength and trajectories when the vortex passes sufficiently near the airfoil to have significant viscous interactions with the airfoil. However, our model shows good agreement with the experimental results when there is sufficient distance between the vortex and the airfoil for the inviscid assumption of the model to hold.

A second comparison is made between the current analytic simulations and a separate experiment by Peng and Gregory (2017) for $\Gamma/(Uc) = -0.196$ (clockwise). Fig. 6(a) compares the incident vortex trajectories from initial locations $y_{\Gamma}(0)/c = \{0.05, -0.05\}$. The large deviations of vortex trajectories observed in Fig. 6(a) are similar to the results in Fig. 5(a) for small separation distances between the vortex and airfoil. We note that the higher vortex initial position $y_{\Gamma}(0)/c = 0.05$ allows the vortex to pass above the airfoil in the experimental measurements, whereas the vortex continues to take a path below the airfoil in the numerical simulation. The abrupt change in vortex path to 'dive' below the oncoming edge was observed experimentally by Ziada and Rockwell (1982) for shear layer impingement on an edge and was modeled analytically by Rogler (1978) for patch vortices encountering a flat plate. Fig. 6(b) shows that the increasing of vortex initial location $\bar{y}_{\Gamma}(0)$ significantly affects the corresponding vortex trajectories. Adjustment of the initial vortex position in the numerical simulation indicates that above $y_{\Gamma}(0)/c = 0.111$, the vortex finally passes above the airfoil and the vortex trajectory offsets downward due to its clockwise direction and its interaction with the airfoil.

3.3. Aeroelastic vortex-airfoil interactions

Attention is now turned to the aeroelastic interactions between the airfoil, the incident, wake and bound vorticity. The investigations are separated into two parts. First, the effects of different lift contributions to the aerodynamic model

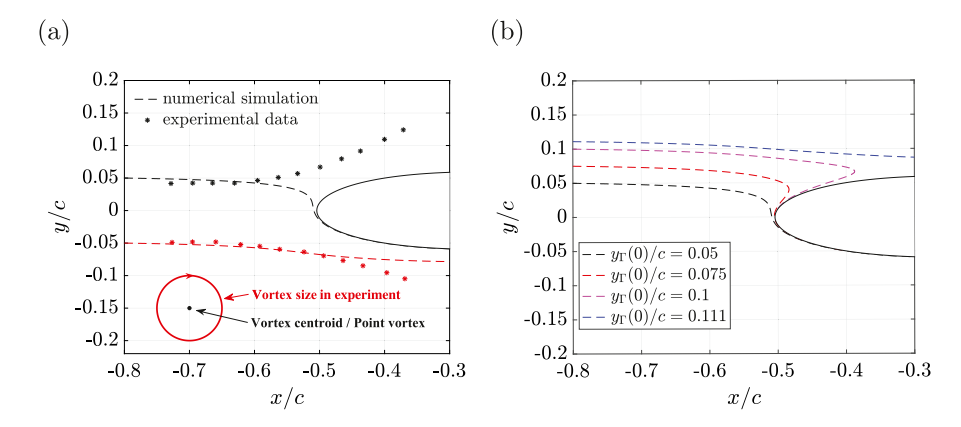


Fig. 6. Comparison of incident vortex gust trajectory near a 12% thickness airfoil against the experiments data of Peng and Gregory (2017, Fig. 9) for $\Gamma/(Uc) = -0.196$ (clockwise). (a) Dependence of vortex trajectory on initial vortex placement. The radius of the vortex core in the experiment is 0.1c. The point vortex does not change its initial strength and is denoted by the dashed line. Asterisks denote averaged experimental data. (b) Computed vortex trajectories from various initial vertical vortex locations.

are examined numerically. Second, the conditions to achieve direct vortex impingement on the airfoil are explored with respect to different aerodynamic parameters.

The linear airfoil suspension described by Eq. (17) introduces additional three dimensionless parameters to the simulations: the reduced natural frequency $\overline{\omega}_n = (2\omega_n\lambda)/U$, the mass ratio $\mu = m/m_{\rm f}$, and the damping ratio $\xi = c_d/(2m\omega_n)$, where $m_{\rm f} = \pi \rho c^2/4$ is the apparent mass of the fluid. The mass ratio is fixed to $\mu = 10$, which is representative of a typical aluminum airfoil in air. The airfoil thickness-to-chord ratio of 12% corresponds to $f_{x0} = -0.092$ in the conformal mapping, and the angle of attack is identically zero. Structural damping is neglected ($\xi = 0$) in all simulations presented.

3.3.1. Comparison of aerodynamic lift contributions in vortex-gust interaction

Per the full unsteady lift expression (18), the unsteady aeroelastic motion of the airfoil is influenced by force contributions from quasi-steady circulatory lift, apparent mass effects, and the unsteady wake. Thus, the effects of the aerodynamic model are assessed for cases of increasing physical sophistication, from the quasi-steady case to the full unsteady case. In this assessment, the reduced natural frequency is set to $\overline{\omega}_n = 0.5$, the initial y-coordinate of the incident vortex is $\overline{y}_{\Gamma}(0) = 0.2$, and the strength of incident vortex is $\overline{\Gamma} = 0.2$. A more complete examination of aerodynamic model assumptions may be carried out over various ranges of $\overline{\omega}_n$, $\overline{y}_{\Gamma}(0)$, and $\overline{\Gamma}$, but such an examination is beyond the scope of this work and is not carried out here.

Fig. 7(a) compares the time variations of the scaled airfoil circulation for all these aerodynamic models. The airfoil circulation history for each model increases with time from the beginning as the incident line vortex approaches to the airfoil and has a sharp change at time $\bar{t}\approx 19.7$. The sharp response results from the strong gust-airfoil interaction of the incident line vortex approaching and passing by the airfoil, after which there is a damped oscillation in the bound circulation (i.e., airfoil lift). In the quasi-steady case, the incident vortex passes by the leading-edge of the airfoil at $\bar{t}=19.24$, and passes by the trailing edge at $\bar{t}=20.03$. Similarly in the added mass case, the incident vortex passes by the leading-edge of the airfoil at $\bar{t}=19.31$, and passes by the trailing edge at $\bar{t}=20.19$, and in the full unsteady case, the incident vortex passes by the leading-edge of the airfoil at $\bar{t}=19.24$, and passes by the trailing edge at $\bar{t}=20.06$. Therefore, the total vortex passage times over the airfoil for the three aerodynamic model variations are $\Delta \bar{t}=0.79$, 0.89, and 0.82, respectively. Moreover, compared to the quasi-steady case, the added mass and full unsteady results have lower-frequency responses in airfoil circulation due to the inclusion of the inertia of the fluid about the airfoil in these cases. Note that the full unsteady case has a stronger initial response to the gust-airfoil interaction and engenders additional aerodynamic damping due to the downwash effect of the wake. Fig. 7(b) shows the time histories of the airfoil displacement for the three aerodynamic model variations, which have a similar response to the airfoil circulation histories in Fig. 7(a).

3.3.2. Vortex impingement

The present scenario fixes the values of the mass ratio $\mu=10$ and the structural damping $\xi=0$. Therefore, the mathematical model is controlled by two dimensionless parameters: the strength of the incident vortex $\overline{\Gamma}$, and the reduced natural frequency of the oscillator $\overline{\omega}_n$. Different initial locations of the incident vortex result in the passage of the incident vortex either above or below the airfoil. Here, the bisection method is used to infer the initial vortex position $\overline{y}_{\Gamma}(0)$ to achieve direct airfoil impingement given $\overline{\Gamma}$ and $\overline{\omega}_n$. The accuracy of $\overline{y}_{\Gamma}(0)$ is controlled by the tolerance of the bisection method, which is set to $\overline{\varnothing}=\varnothing/(2\lambda)=0.01$ in the present work. Fig. 8 shows the incident vortex trajectories for different

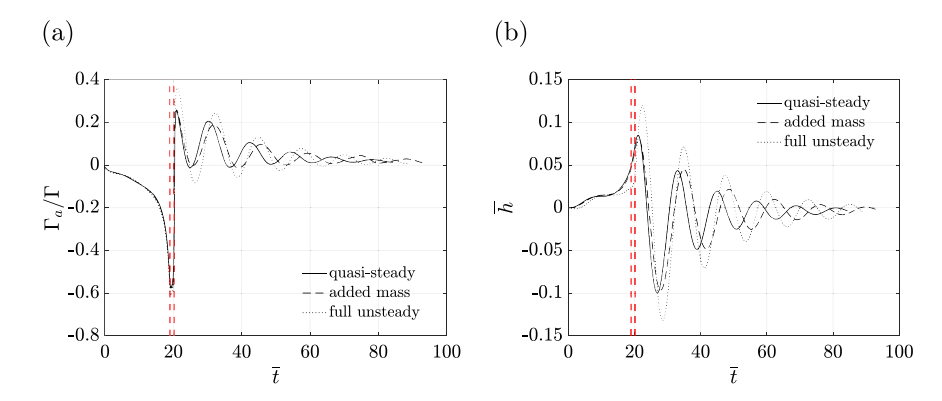


Fig. 7. Comparisons of time histories of (a) scaled airfoil circulation and (b) airfoil displacement for different cases of lift contribution: quasi-steady case added mass case, and full unsteady case. Vertical lines represent the intervals in time when the incident vortex passes by the airfoil leading and trailing edges. $\overline{\omega}_n = 0.5$, $\overline{y}_{\Gamma}(0) = 0.2$, and $\overline{\Gamma} = 0.2$.

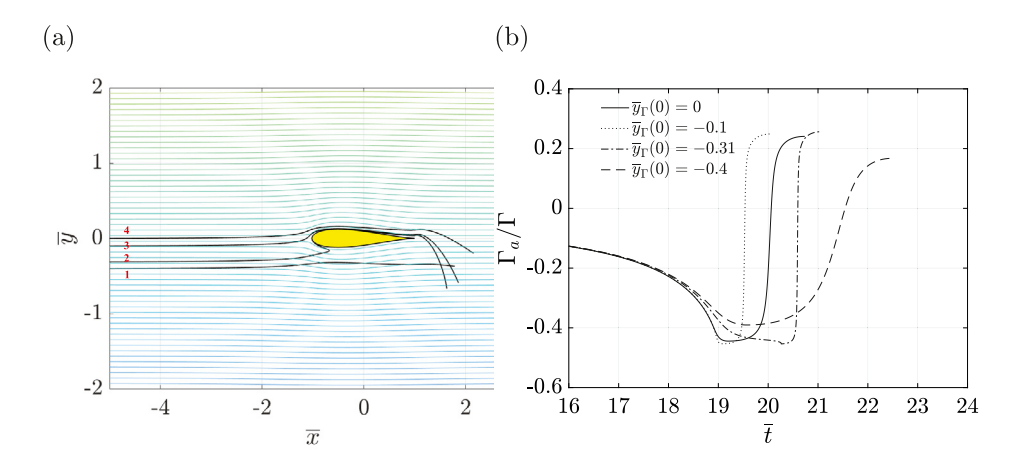


Fig. 8. Time histories of incident vortex trajectories and the bound circulation for different initial vortex positions, with reduced natural frequency $\overline{\omega}_n = 0.5$ and incident vortex strength $\overline{\Gamma} = 0.1$: (a) time-varying trajectories of the incident line vortex Γ (denoted 1, 2, 3, 4) resulting from an incident vortex Γ with different initial positions $y_{\Gamma}(0) = \{-0.4, -0.3, -0.1, 0\}$ past a symmetrical Joukowski airfoil with 12% thickness. The streamlines in the flow field are for the case when all vortices are absent, and the motion of the incident vortex across these lines under the influence of the airfoil is noted. (b) Time variations of corresponding bound circulation on the airfoil during the shedding of the first two trailing-edge vortices.

initial vortex positions and the corresponding time histories of the airfoil circulation. Fig. 8(a) plots the trajectories of the incident vortex in the aeroelastic simulations with different initial locations, atop the steady streamlines of the flow field in the absence of vortices for visual reference. For $y_{\Gamma}(0) = -0.4$, the incident vortex follows initially the steady streamline from the left inflow locations and moves below the airfoil at large times. As the initial location moves up to the impingement location $y_{\Gamma}(0) = -0.31$, the incident vortex aligns with the steady streamline at early times. However, near the airfoil, the vortex path deviates backward under influence of the shed vorticity and airfoil motion and moves along a path near the stagnation streamline at the airfoil. As the initial location of the incident vortex moves upward, smaller deviation of the path of the incident vortex is observed in Fig. 8(a).

Fig. 8(b) presents time variations of the airfoil circulation that occur over the initial time period where only the first two trailing-edge vortices are shed. For the cases when the initial vortex location is $y_{\Gamma}(0) = \{0, -0.1\}$, which cause the incident vortex to move above the airfoil, the corresponding magnitudes of the airfoil circulation time histories increase similarly at early times. These time histories have a sharp change when the incident vortex passes closest to the airfoil due to the shedding of the second vortex. However, for the case when the initial vortex moves below the airfoil, a smaller peak-to-peak value and an extended flat response in the airfoil circulation with respect to time is observed in Fig. 8(b), which may infer a weak interaction between the incident vortex and the airfoil. The initial vortex location $y_{\Gamma}(0) = -0.31$ that results in vortex impingement demonstrates a similar flat circulation response. However, the shedding of the second vortex is delayed when the incident vortex passes near the stagnation streamline at the airfoil.

The effects of different aeroelastic parameters such as $\overline{\Gamma}$ and $\overline{\omega}_n$ are now studied with respect to the selection of initial incident vortex locations to achieve vortex impingement. In the current numerical scheme, vortex impingement commonly occurs while only the first trailing-edge vortex exists and has convected downstream of the airfoil, where

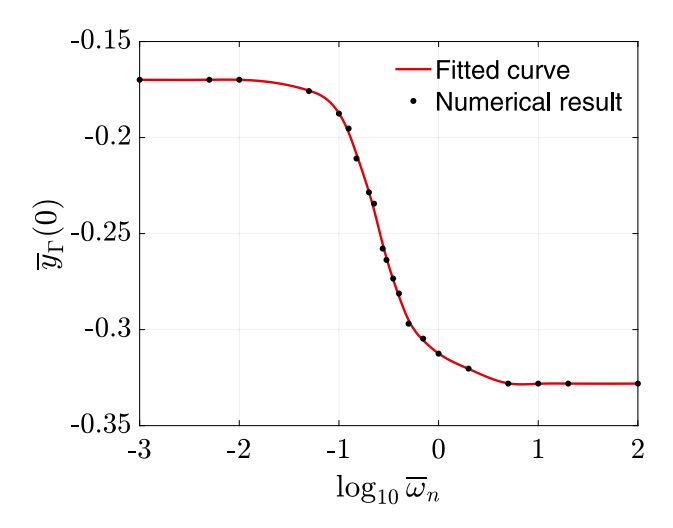


Fig. 9. Effect of reduced natural frequency $\overline{\omega}_n$ on the initial incident vortex vertical position $\overline{y}_{\Gamma}(0)$ to achieve direct airfoil impingement. Incident vortex has a strength of $\overline{\Gamma}=0.1$ and moves past a symmetric Joukowski airfoil with 12% thickness.

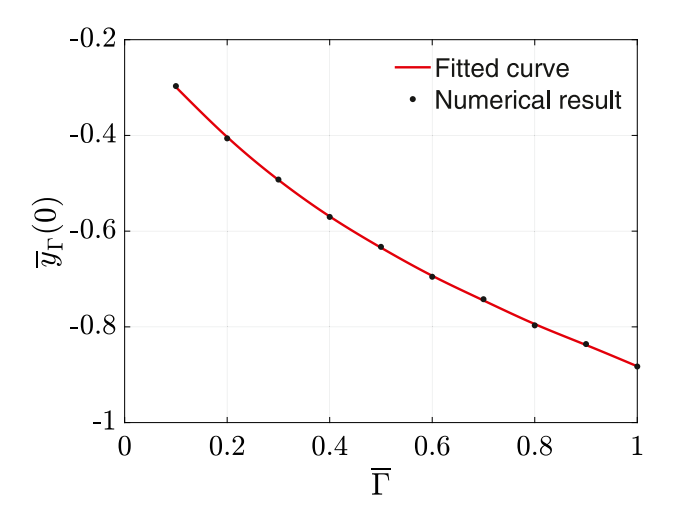


Fig. 10. Variations of selection of initial incident vortex location $\bar{y}_{\Gamma}(0)$ with varying strength of incident vortex $\overline{\Gamma}$ when vortex impingement occurs, with reduced natural frequency $\overline{\omega}_n = 0.5$.

its downwash effect on the airfoil may be neglected. Fig. 9 presents results for the vortex initial vertical position to achieve direct airfoil impingement as a function for $\overline{\omega}_n$ for $\overline{\Gamma}=0.1$. In these simulations, the downwash effect of the airfoil wake has been neglected in the aerodynamic model. It is clear from Fig. 9 that there are upper and lower asymptotic limits on the initial vertical vortex positions to have impingement, where $\overline{y}_{\Gamma}(0) \to -0.17$ for small values of $\overline{\omega}_n$ and $\overline{y}_{\Gamma}(0) \to -0.328$ for large values. Recalling that these simulations are performed at fixed mass ratio and without structural damping, the lower and upper limits correspond to negligible spring restoring force (free airfoil) and dominant spring (rigid support) limits. Importantly, the results demonstrate a monotonic change in initial vortex position $\overline{y}_{\Gamma}(0)$ with respect to the reduced natural frequency for a given value, and these values of $\overline{y}_{\Gamma}(0)$ are bounded by the low and high frequency limits of $\overline{\omega}_n$.

Lastly, Fig. 10 determines $\overline{y}_{\Gamma}(0)$ for impingement for fixed reduced frequency $\overline{\omega}_n=0.5$ as a function of the incident vortex strength Γ . The value the initial vertical position of the incident vortex decreases monotonically with increasing Γ and indicates the need for lower vortex positioning for direct impingement for stronger incident vortices.

Some additional commentary is warranted at this point with respect to the validity of this inviscid model to predict vortex impingement conclusions accurately for real fluids. A comparison of the present model against the airfoil experiments in Section 3.2 indicates clearly that the airfoil boundary layer has a strong influence on the trajectories of vortices passing closely above or below the airfoil. However, it remains unclear what influence if any the boundary layer has the conditions for direct impingement for fixed or aeroelastic airfoil. Companion experimental efforts to test the validity of the present model predictions would be valued but have not yet conducted to the authors' knowledge.

4. Conclusions

An analytical system of equations is developed to simulate numerically the aeroelastic interactions of an incident line vortex with a Joukowski airfoil on a linear elastic suspension. The mathematical framework is modeled by using dynamic conformal mapping techniques. The dynamical problem for the incident vortex motion and trailing edge wake evolution is studied using potential flow theory and the Brown and Michael equation for vortices shed from the airfoil trailing edge.

Numerical simulations of the analytical model are verified in the limiting cases of stationary and harmonically-plunging flat plates, and the effect of airfoil thickness on the vortex gust interaction is systematically examined for stationary, symmetric Joukowski airfoils. Comparisons of the numerical solutions against vortex gust interaction data for fixed real airfoils indicate good agreement for vortex path prediction when the incident vortex is sufficiently far from the airfoil to have mild to negligible viscous interactions with the airfoil and its boundary layer. However, the numerical agreement of vortex path predictions is increasingly poor for incident vortex positions closer to the airfoil. The change in strength of the incident vortex due to viscous effects of the airfoil boundary layer that was identified by Peng and Gregory (2015) is shown to be a good indicator of the degree of violation of the inviscid model assumptions and of the disagreement between the model and experimental observation.

The influence of lift contributions in the aerodynamic model are assessed in the context of the aeroelastic vortex gust-airfoil framework. The aeroelastic results of all three aeroelastic models of increasing sophistication (quasi-steady, added mass, and full unsteady) demonstrate an oscillatory damping of airfoil circulation and plunge displacement in long times in the absence of structural damping. The full unsteady case adds more aerodynamic damping to the aeroelastic model and imparts a larger impulse to the airfoil circulation and structural response from its gust encounter relative to other variations of the aerodynamic model that is due to the unsteady wake contribution to the lift.

The aeroelastic framework is then used to determine the conditions for achieving direct impingement of an incident line vortex with the elastically-mounted airfoil. The aeroelastic results of a symmetric Joukowski airfoil with 12% thickness-to-chord ratio demonstrate that the incident vortex follows initially the steady streamline in the uniform flow, but deviates backward and then moves along a path near the stagnation streamline at the airfoil near where the vortex impingement occurs. The initial vortex placement for airfoil impingement changes monotonically with the reduced natural frequency in a specific range that depends on the vortex strength. However, for fixed incident vortex strength, asymptotic limits on the vortex placement to achieve impingement are discussed numerically in the limits of high and low reduced natural frequency of the elastic suspension. Therefore, there is a finite range of vortex positions where vortex impingement occurs for aeroelastic vortex gust encounters that depends upon the strength of the incident vortex. Companion experimental comparisons of aeroelastic vortex—airfoil interactions and the associated fluid effects on impingement prediction have not yet been carried out to the authors' knowledge and are desired for validation and to identify any necessary improvements to the physics modeling.

CRediT authorship contribution statement

Huansheng Chen: Conceptualization, Methodology, Software, Validation, Formal analysis, Writing - original draft, Visualization. **Justin W. Jaworski:** Writing - review & editing, Supervision, Funding acquisition.

Declaration of competing interest

The authors declare that they have no known competing financial interests or personal relationships that could have appeared to influence the work reported in this paper.

Acknowledgments

This work was supported in part by the Air Force Office of Scientific Research, United States of America under AFOSR grants FA9550-15-1-0148 and FA9550-19-1-0095, monitored by Drs. Douglas Smith and Gregg Abate, and by the National Science Foundation, United States of America under awards 1805692 and 1846852, monitored by Dr. Ronald Joslin. Preliminary results from this paper were presented as parts of AIAA Papers 2018-2907 (Chen and Jaworski, 2018) and 2019-0897 (Chen and Jaworski, 2019). This research was carried out in coordination with the NATO AVT-282 task group entitled "Unsteady Aerodynamic Response of Rigid Wings in Gust Encounters". Constructive feedback on this work by members of this task group is gratefully acknowledged.

Appendix A. Scalar form of emended Brown and Michael equation

The original emended Brown and Michael equation is Howe (1996)

$$\frac{\mathrm{d}\boldsymbol{x}_{\gamma_n}}{\mathrm{d}t} \cdot \nabla \Psi_i + \frac{\Psi_i}{\gamma_n} \frac{\mathrm{d}\gamma_n}{\mathrm{d}t} = \boldsymbol{v}_{\gamma_n} \cdot \nabla \Psi_i, \qquad i = 1, 2. \tag{22}$$

Eq. (22) can be reexpressed in vector format as

$$\left(\frac{\mathrm{d}x}{\mathrm{d}t}, \frac{\mathrm{d}y}{\mathrm{d}t}\right) \cdot \left(\frac{\partial \Psi_1}{\partial x}, \frac{\partial \Psi_1}{\partial y}\right) + \frac{\Psi_1}{\gamma_n} \frac{\mathrm{d}\gamma_n}{\mathrm{d}t} = \left(v_x, v_y\right) \cdot \left(\frac{\partial \Psi_1}{\partial x}, \frac{\partial \Psi_1}{\partial y}\right), \tag{23}$$

$$\left(\frac{\mathrm{d}x}{\mathrm{d}t}, \frac{\mathrm{d}y}{\mathrm{d}t}\right) \cdot \left(\frac{\partial \Psi_2}{\partial x}, \frac{\partial \Psi_2}{\partial y}\right) + \frac{\Psi_2}{\gamma_n} \frac{\mathrm{d}\gamma_n}{\mathrm{d}t} = \left(v_x, v_y\right) \cdot \left(\frac{\partial \Psi_2}{\partial x}, \frac{\partial \Psi_2}{\partial y}\right), \tag{24}$$

which can be also expanded respectively as

$$\frac{\mathrm{d}x}{\mathrm{d}t}\frac{\partial\Psi_{1}}{\partial x} + \frac{\mathrm{d}y}{\mathrm{d}t}\frac{\partial\Psi_{1}}{\partial y} + \frac{\Psi_{1}}{\gamma_{n}}\frac{\mathrm{d}\gamma_{n}}{\mathrm{d}t} = v_{x}\frac{\partial\Psi_{1}}{\partial x} + v_{y}\frac{\partial\Psi_{1}}{\partial y},\tag{25}$$

$$\frac{\mathrm{d}x}{\mathrm{d}t}\frac{\partial\Psi_2}{\partial x} + \frac{\mathrm{d}y}{\mathrm{d}t}\frac{\partial\Psi_2}{\partial y} + \frac{\Psi_2}{\gamma_n}\frac{\mathrm{d}\gamma_n}{\mathrm{d}t} = v_x\frac{\partial\Psi_2}{\partial x} + v_y\frac{\partial\Psi_2}{\partial y}.$$
 (26)

From Eqs. (25) and (26), the general scalar form of emended Brown and Michael equation may be written as

$$\frac{\mathrm{d}x}{\mathrm{d}t} + H_1 \frac{1}{\gamma_n} \frac{\mathrm{d}\gamma_n}{\mathrm{d}t} = v_x,\tag{27}$$

$$\frac{\mathrm{d}y}{\mathrm{d}t} + H_2 \frac{1}{\gamma_n} \frac{\mathrm{d}\gamma_n}{\mathrm{d}t} = v_y,\tag{28}$$

where

$$H_1 = \frac{\Psi_1 \frac{\partial \Psi_2}{\partial y} - \Psi_2 \frac{\partial \Psi_1}{\partial y}}{\frac{\partial \Psi_1}{\partial x} \frac{\partial \Psi_2}{\partial y} - \frac{\partial \Psi_2}{\partial x} \frac{\partial \Psi_1}{\partial y}},\tag{29}$$

$$H_2 = \frac{\Psi_1 \frac{\partial \Psi_2}{\partial x} - \Psi_2 \frac{\partial \Psi_1}{\partial x}}{\frac{\partial \Psi_1}{\partial y} \frac{\partial \Psi_2}{\partial y} - \frac{\partial \Psi_2}{\partial y} \frac{\partial \Psi_1}{\partial y}}.$$
 (30)

Expressions (27) and (28) can be combined using $z_{\gamma_n}^* = x - iy$, and $v_{\gamma_n}^* = v_x - iv_y$ to create the complex-valued scalar form of the emended Brown and Michael equation:

$$\frac{\mathrm{d}z_{\gamma_n}^*}{\mathrm{d}t} + (H_1 - iH_2) \frac{1}{\gamma_n} \frac{\mathrm{d}\gamma_n}{\mathrm{d}t} = v_{\gamma_n}^*. \tag{31}$$

Once the stream function Ψ_i (i=1,2) is known, it is possible to determine $\nabla \Psi_i = (\partial \Psi_i/\partial x, \partial \Psi_i/\partial y)$. Thus, H_1 and H_2 are known, and the vortex motion can be analyzed from Eq. (31).

Appendix B. Verification of simulations

Consider the degenerate case of the generalized model in Fig. 1 that results in a rigid, flat plate of length 4λ immersed in a uniform flow with speed U in the x-direction. An incident line vortex of constant strength Γ is released into the flow at the initial instant in time (t=0) and passes near the airfoil. The airfoil moves harmonically in the y-direction with the prescribed heaving motion

$$h(t) = \varepsilon \lambda \cos(\omega t), \qquad t > 0,$$
 (32)

where $\varepsilon \ll 1$ and ω is the frequency of the heaving motion. Vortex shedding is produced to satisfy the Kutta condition at the trailing edge of the airfoil. In this problem, we consider multiple vortices shedding which is discretized as a set of line vortices whose positions $z_{\gamma_n} = x_{\gamma_n} + iy_{\gamma_n}$ (n = 1, 2, 3, ...) and strengths γ_n (n = 1, 2, 3, ...) change with time. This scenario has been previously investigated by Manela (2013) and furnishes a verification case for the more general framework developed in this paper.

The dimensionless parameters and initial conditions replicate those in Manela (2013) to furnish a direct comparison: $\bar{x} = x/(2\lambda)$, $\bar{y} = y/(2\lambda)$, $\bar{t} = Ut/(2\lambda)$, $\bar{\omega} = \omega(2\lambda)/U$ and $\bar{\Gamma} = \Gamma/(4\pi U\lambda)$. For a flat plate airfoil, the center f_0 in Eq. (2) is set to the origin, and the initial line-vortex location is $\bar{z}_{\Gamma}(0) = (-20, 0.2)$. The strength of the incident vortex is $\bar{\Gamma} = 0.2$. As also observed by Howe (1996), the numerical results are insensitive to this initial placement provided it is sufficiently near the edge. Initial placements of the vortex within a non-dimensional distance of $O(10^{-3})$ to the trailing-edge did not affect the present numerical results. However, at the instant when a new point vortex is produced at the trailing edge vortex, the Brown and Michael equation has a singularity that can affect numerical simulations with very small time steps. Michelin and Llewellyn Smith (2009) resolve this issue by solving analytically for the motion of the shed vortex in its first time step using the analysis of Cortelezzi (1995). This correction has not been incorporated here and was found to not be necessary in the present simulations to achieve numerical convergence.

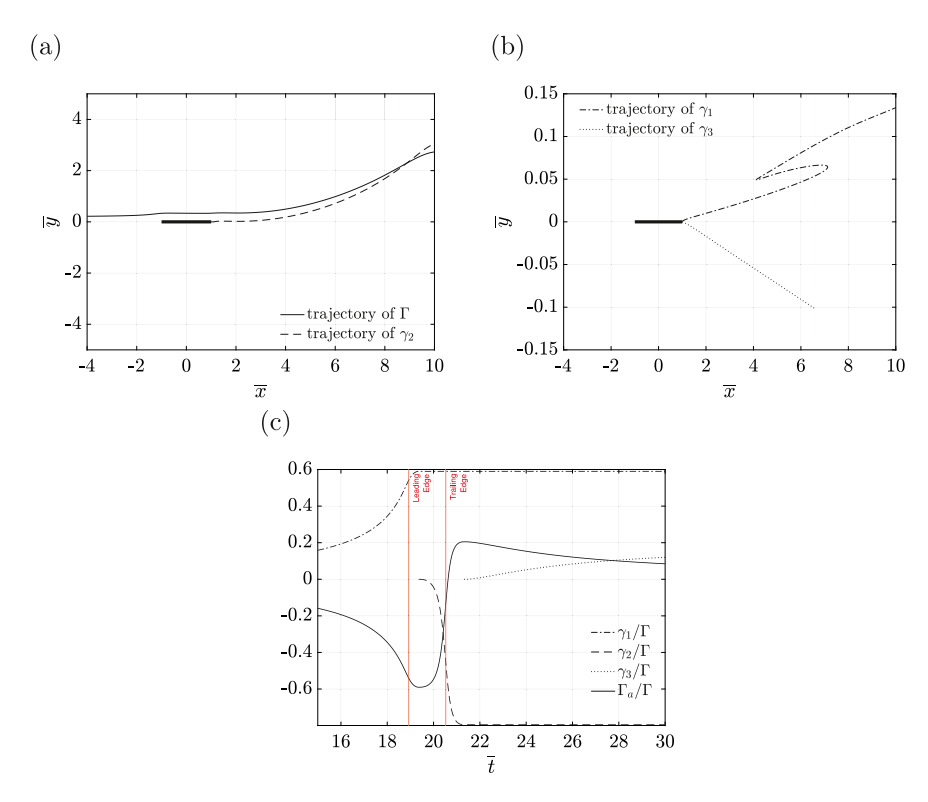


Fig. 11. Trajectories of an incident line vortex Γ and three shed vortices γ_1 , γ_2 , and γ_3 from a stationary flat plate airfoil in uniform flow: (a) trajectories of incident vortex Γ and trailing edge vortex γ_2 ; (b) trajectories of trailing edge vortices γ_1 and γ_3 ; (c) circulation of the airfoil and trailing edge vortices in time. The passage of the incident vortex past the leading and trailing edges is indicated by the vertical dashed lines.

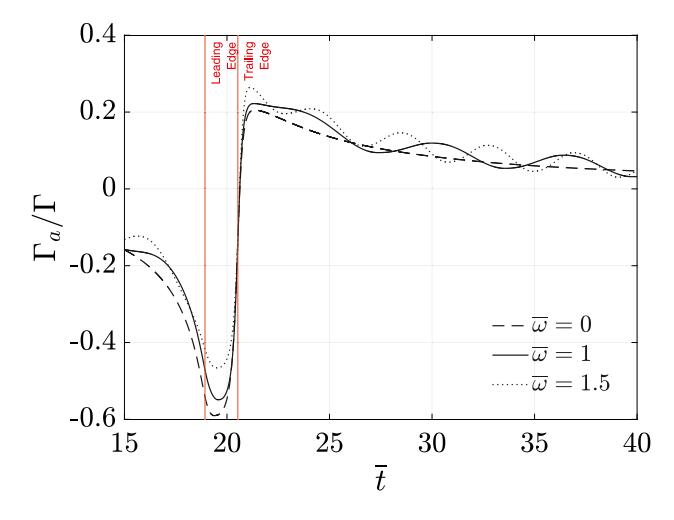


Fig. 12. Time histories of scaled airfoil circulation for different frequencies of prescribed heaving motions of a flat plate with $\epsilon=0.01$.

B.1. Stationary flat plate

When the flat plate airfoil is stationary ($\varepsilon = 0$), the numerical results of the vortex-interaction indicate that $d\gamma_3/dt$ does not change sign after the third vortex is shed from the trailing edge. Therefore, the trailing edge wake can be described by only three trailing-edge vortices shed into the wake under the emended Brown and Michael framework. Numerical

results for the trajectories of the three shed vortices and their strengths are illustrated in Fig. 11 and replicate Fig. 2 of Manela (2013).

B.2. Flat plate under prescribed plunging motion

motion. J. Fluids Struct. 62, 230-251.

Rockwell, D.O., 1998. Vortex-body interactions. Annu. Rev. Fluid Mech. 30, 199-229.

Rott, N., 1956. Diffraction of a weak shock with vortex generation. J. Fluid Mech. 1 (1), 111-128.

Ziada, S., Rockwell, D., 1982. Vortex-leading-edge interaction. J. Fluid Mech. 118, 79-107.

Rockwell, D., Knisely, C., 1979. The organized nature of flow impingement upon a corner. J. Fluid Mech. 93 (3), 413-432.

Rogler, H., 1978. The interaction between vortex-array representations of free-stream turbulence and semi-infinite flat plates. J. Fluid Mech. 87 (3),

Tchieu, A.A., Leonard, A., 2011. A discrete-vortex model for the arbitrary motion of a thin airfoil with fluidic control. J. Fluids Struct. 27 (5–6), 680–693.

Wang, C., Eldredge, J.D., 2013. Low-order phenomenological modeling of leading-edge vortex formation. Theor. Comput. Fluid Dyn. 27 (5), 577–598.

For a flat plate is under prescribed harmonic heaving motion ($\varepsilon = 0.01$), the results shown in Fig. 12 verify and replicate Fig. 4(d) in Manela (2013).

References

Baddoo, P.J., Ayton, L.J., 2018. Vortex equilibria in ground effect. In: 2018 AIAA Fluid Dynamics Conference. Paper AIAA-2018-2903. Barnes, C.J., Visbal, M.R., 2018a. Clockwise vortical-gust/airfoil interactions at a transitional Reynolds number. AIAA J. 56 (10), 3863-3874. Barnes, C.I., Visbal, M.R., 2018b. Counterclockwise vortical-gust/airfoil interactions at a transitional Reynolds number. AIAA J. 56 (7), 2540-2552. Batchelor, G.K., 1967. An Introduction to Fluid Dynamics. Cambridge University Press, United Kingdom. Bisplinghoff, R.L., Ashley, H., Halfman, R.L., 1996. Aeroelasticity, first ed. Dover Publications, Inc., New York. Brown, C.E., Michael, W.H., 1954. Effect of leading-edge separation on the lift of a delta wing. J. Aeronaut. Sci. 21 (10), 690–694. Brown, C.E., Michael, W.H., 1955. On Slender Delta Wings with Leading-Edge Separation. Tech. Rep. TN 3430, NACA. Chen, H., Jaworski, J.W., 2018. Vortex interactions with Joukowski airfoil on elastic supports. In: AIAA Fluid Dynamics Conference, Atlanta, GA. Paper AIAA-2018-2907. Chen, H., Jaworski, J.W., 2019. Aeroelastic trajectory selection of vortex gusts impinging upon Joukowski airfoils. In: AIAA SciTech Forum. AIAA-2019-0897. Cheng, H.K., 1954. Remarks on nonlinear lift and vortex separation. J. Aeronaut. Sci. 21 (3), 212-214. Clements, R., 1973. An inviscid model of two-dimensional vortex shedding. J. Fluid Mech. 57 (2), 321-336. Conlisk, A., Rockwell, D., 1981. Modeling of vortex-corner interaction using point vortices. Phys. Fluids 24 (12), 2133-2142. Conlisk, A.T., Veley, D., 1985. The generation of noise in impinging vortex motion past a step. Phys. Fluids 28 (10), 3004-3012. Cortelezzi, L., 1995. On the unsteady separated flow past a semi-infinite plate: exact solution of the Brown and Michael model, scaling, and universality. Phys. Fluids 7 (3), 526-529. Crighton, D.G., 1972. Radiation from vortex filament motion near a half plane. J. Fluid Mech. 51 (2), 357-362. Crowdy, D., 2010. A new calculus for two-dimensional vortex dynamics. Theor. Comput. Fluid Dyn. 24 (1-4), 9-24. Darakananda, D., Eldredge, J.D., 2019. A versatile taxonomy of low-dimensional vortex models for unsteady aerodynamics. J. Fluid Mech. 858, 917-948. Doligalski, T.L., Smith, C.R., Walker, J.D.A., 1994. Vortex interactions with walls. Annu. Rev. Fluid Mech. 26 (1), 573-616. Edwards, R.H., 1954. Leading-edge separation from delta wings. J. Aeronaut. Sci. 21 (2), 134-135. Eldredge, J.D., Jones, A.R., 2019. Leading-edge vortices: mechanics and modeling. Annu. Rev. Fluid Mech. 51, 75-104. Glauert, H., 1983. The Elements of Aerofoil and Airscrew Theory. Cambridge University Press, United Kingdom. Graham, J.M.R., 1977. Vortex Shedding from Sharp Edges. Tech. Rep. 77-06, Imperial College Department of Aeronautics. Graham, J.M.R., 1980. The forces on sharp-edged cylinders in oscillatory flow at low Keulegan-Carpenter numbers. J. Fluid Mech. 97 (2), 331-346. Gursul, I., Rockwell, D., 1990. Vortex street impinging upon an elliptical leading edge. J. Fluid Mech. 211, 211-242. Howe, M.S., 1994. Elastic blade-vortex interaction noise. J. Sound Vib. 177 (3), 325-336. Howe, M.S., 1996. Emendation of the Brown & Michael equation, with application to sound generation by vortex motion near a half-plane. J. Fluid Mech. 329, 89-101. Howe, M.S., 1997. Influence of separation on sound generated by vortex-step interaction. J. Fluids Struct. 11 (8), 857-872. Howe, M.S., 2003. Theory of Vortex Sound, Vol. 33. Cambridge University Press, United Kingdom. Howe, M.S., 2014. Acoustics and Aerodynamic Sound. Cambridge University Press, United Kingdom. Jaworski, J.W., 2016. Vortex sound generation from flexible fibers. In: 22nd AIAA/CEAS Aeroacoustics Conference, Lyon, France. Paper AIAA-2016-2752. Jaworski, J.W., 2018. Hydroelastic motions of flexible fibers. In: 2018 AIAA/CEAS Aeroacoustics Conference, Atlanta, GA. Paper AIAA-2018-3786. Jaworski, J.W., 2019. Sound from aeroelastic vortex-fibre interactions. Philos. T. R. Soc. A 377 (2159), 20190071. von Kármán, T., Sears, W.R., 1938. Airfoil theory for non-uniform motion. J. Aeronaut. Sci. 5 (10), 379-390. Katz, J., Plotkin, A., 2001. Low-Speed Aerodynamics, second ed. Cambridge University Press, United Kingdom. Lee, D.J., Smith, C.A., 1991. Effect of vortex core distortion on blade-vortex interaction. AIAA J. 29 (9), 1355-1362. Manela, A., 2011. Sound generated by a vortex convected past an elastic sheet. J. Sound Vib. 330 (3), 416-430. Manela, A., 2013. Nonlinear effects of flow unsteadiness on the acoustic radiation of a heaving airfoil. J. Sound Vib. 332 (26), 7076-7088. Manela, A., Huang, L., 2013. Point vortex model for prediction of sound generated by a wing with flap interacting with a passing vortex. J. Acoust. Soc. Am. 133 (4), 1934-1944. Michelin, S., Llewellyn Smith, S.G., 2009. An unsteady point vortex method for coupled fluid-solid problems. Theor. Comput. Fluid Dyn. 23 (2), 127-153. Newton, P.K., 2013. The N-Vortex Problem: Analytical Techniques, Vol. 145. Springer. Panaras, A.G., 1987. Numerical modeling of the vortex/airfoil interaction. AIAA J. 25 (1), 5-11. Peng, D., Gregory, J.W., 2015. Vortex dynamics during blade-vortex interactions. Phys. Fluids 27 (5), 053104. Peng, D., Gregory, J.W., 2017. Asymmetric distributions in pressure/load fluctuation levels during blade-vortex interactions. J. Fluids Struct. 68, 58-71. Peters, M.C.A.M., Hirschberg, A., 1993. Acoustically induced periodic vortex shedding at sharp edged open channel ends; simple vortex models. J. Sound Vib. 161 (2), 281-299. Riso, C., Riccardi, G., Mastroddi, F., 2016. Nonlinear aeroelastic modeling via conformal mapping and vortex method for a flat-plate airfoil in arbitrary